Structural insights into the functional cycle of the ATPase module of the 26S proteasome

Marc Wehmer[a,1], Till Rudack[b,1], Florian Beck[a,1], Antje Aufderheide[a], Günter Pfeifer[a], Jürgen M. Plitzko[a], Friedrich Förster[a,c], Klaus Schulten[b,2], Wolfgang Baumeister[a,3], and Eri Sakata[a,3]

[a]Department of Molecular Structural Biology, Max Planck Institute of Biochemistry, 82152 Martinsried, Germany; [b]Beckman Institute, Center for the Physics of Living Cells, University of Illinois, Urbana–Champaign, Urbana, IL 61801; and [c]Bijvoet Center for Biomolecular Research, Utrecht University, 3584 CH Utrecht, The Netherlands

In eukaryotic cells, the ubiquitin–proteasome system (UPS) is responsible for the regulated degradation of intracellular proteins. The 26S holocomplex comprises the core particle (CP), where proteolysis takes place, and one or two regulatory particles (RPs). The base of the RP is formed by a heterohexameric AAA+ ATPase module, which unfolds and translocates substrates into the CP. Applying single-particle cryo-electron microscopy (cryo-EM) and image classification to samples in the presence of different nucleotides and nucleotide analogs, we were able to observe four distinct conformational states (s1 to s4). The resolution of the four conformers allowed for the construction of atomic models of the AAA+ ATPase module as it progresses through the functional cycle. In a hitherto unobserved state (s4), the gate controlling access to the CP is open. The structures described in this study allow us to put forward a model for the 26S functional cycle driven by ATP hydrolysis.

26S proteasome | cryo-electron microscopy | AAA+ ATPase | integrative modeling | single-particle analysis

In eukaryotic cells, the ubiquitin–proteasome system (UPS) degrades proteins that are misfolded, damaged, or no longer needed (1). The 26S proteasome is a 2.5-MDa multisubunit complex comprising the barrel-shaped 20S core particle (CP), where degradation takes place, and one or two 19S regulatory particles (RPs), which bind to the ends of the CP (2–4). The CP is built of four coaxially stacked heteroheptameric rings of α- and β-subunits in the order of αββα (5). Three of the seven β-subunits are catalytically active; substrates are sequestered from the cellular environment in a chamber formed by the two β-rings (6, 7). This self-compartmentalization is a hallmark of many intracellular proteases (8). Substrate access to the proteolytic chamber is controlled by the α-subunit N-terminal extensions, forming a gate (3). Most of proteasome activators, including the RP, contain C-terminal hydrophobic-tyrosine-X (HbYX) motifs, which have been reported to insert into α-ring pockets, triggering gate opening (9–11).

The RP is composed of at least 19 canonical subunits and interacts substoichiometrically with an array of proteasome-interacting proteins that modulate RP function (3). The RP is divided into the "base" and the "lid" subcomplexes. The core of the base is formed by a heterohexameric ATPase associated with various cellular activities (AAA+ ATPase), which is the driver of large-scale conformational dynamics of the RP. The AAA+ ATPase prepares substrates for degradation in coordination with at least three ubiquitin receptors [26S proteasome non-ATPase regulatory subunit 1 (Rpn1), Rpn10, and Rpn13] (12–14) and a deubiquitylating subunit (Rpn11) (15, 16). Other subunits have structural roles, such as holding the CP and RP together, or in coordinating the movements needed to position the substrates above the pore of the AAA+ ATPase for unfolding and translocation (17, 18). The AAA+ ATPase is lined by aromatic-hydrophobic loops (pore-1 loops), which grab and pull polypeptides. Driven by ATP binding and hydrolysis, the pore-1 loops undergo conformational changes threading the polypeptide through the central channel, similar to the mechanism postulated for the bacterial

ATP-dependent caseinolytic protease X (ClpX) (19, 20). Our previous study revealed the existence of three distinct conformational states (21). According to their putative functions, these states were referred to as a substrate-accepting state (s1), a commitment state (s2), and a substrate-processing state (s3). The major structural differences between these states are the coaxial alignment of the AAA+ ATPase with the CP and a rotary movement of the deubiquitylating module into a position enabling deubiquitylation. Recently, several single-particle cryo-electron microscopy (cryo-EM) studies have described the architecture of the yeast and human proteasome (22–25). In the presence of ATP, the majority of the proteasomes are in an s1 or s1-like state. More states are likely to exist, but they were not sufficiently populated to yield high-resolution structures, and therefore precluded a detailed understanding of the relationship between the nucleotide-bound states and the observed conformational changes.

Here, we report cryo-EM structures of the yeast 26S proteasome in the presence of different nucleotides and nucleotide analogs, revealing the existence of four distinct conformational states. These structures elucidate the conformational changes underlying substrate translocation and their coupling with gate opening.

Significance

The 26S proteasome is a large multisubunit complex that executes the degradation of intracellular proteins marked for destruction by ubiquitylation. To understand the mechanistic details of the functional cycle of the 26S proteasome, it is necessary to elucidate the structural features of its "engine," the AAA+ ATPase module, which unfolds and translocates substrates into the 20S core particle, where proteolysis takes place. Here, we report cryo-electron microscopy reconstructions of the yeast 26S proteasome in the presence of different nucleotides and nucleotide analogs. Our results provide structural insights into the mechanism of substrate unfolding and translocation by the 26S proteasome.

BIOCHEMISTRY

Results

High-Resolution Structures of Yeast 26S Proteasome in the Presence of ATP. To obtain a high-resolution 3D map, images of vitrified yeast 26S proteasomes in the presence of 4 mM ATP were recorded (Fig. S1*A* and Table S1). After elimination of low-quality particles (Fig. S1 *B* and *C*), the proteasome particles were classified according to the RP states (22, 26). Ultimately, we obtained maps of the s1 and s2 states to global resolutions of 4.1 Å and 4.5 Å, respectively (Fig. 1 *A* and *B* and Fig. S1*F*). Similar to the human 26S proteasome (22), the CP exhibited local resolution values beyond 1/4 Å^{-1}, whereas the RP, especially the peripheral regions, was resolved at lower than 1/8 Å^{-1} (Fig. S1 *G* and *H*).

We first built the model of the s1 state from a comparative model based on the human 26S proteasome structure (22). The s2 model was obtained by molecular dynamics flexible fitting (MDFF) (27) of the s1 model into the s2 map. The s1 and s2 structures are overall similar to the previous models based on low-resolution densities (21), but they exhibit subtle structural differences, such as the register shifts as described by Schweitzer et al. (22). These differences include a kink in the 26S proteasome ATPase regulatory subunit 1/2 (Rpt1/2) N-terminal coiled coil (Rpt1 Gly68 to Pro78, Rpt2 Ile81 to Pro84), which was not found in the other two coiled coils (Rpt3/6 and Rpt4/5).

Despite the overall lower resolution, Rpn13 is better resolved in the s2 state than in the s1 state. The structure and motion of this subunit were analyzed further by focused classification. An exhaustive 6D correlation search in the best-resolved class (Fig. S2*A*) resulted in an unambiguous positioning of Rpn13. Cross-linking mass spectrometry (MS) data validated this positioning (Table S2). In comparison to the previous model (21), Rpn13 is rotated by ~105°, so that the Rpn2-binding region of Rpn13 points toward Rpn2 (28) and fulfills the cross-linking restraints.

Structures of 26S in the Presence of Different Nucleotide Analogs. To detect additional conformations of the RP, we analyzed structures of the 26S proteasome in the presence of different nucleotides and nucleotide analogs [adenylyl-imidodiphosphate (AMP-PNP), ATP/ADP + beryllium fluoride (BeF$_x$), and ADP] (Table S1).
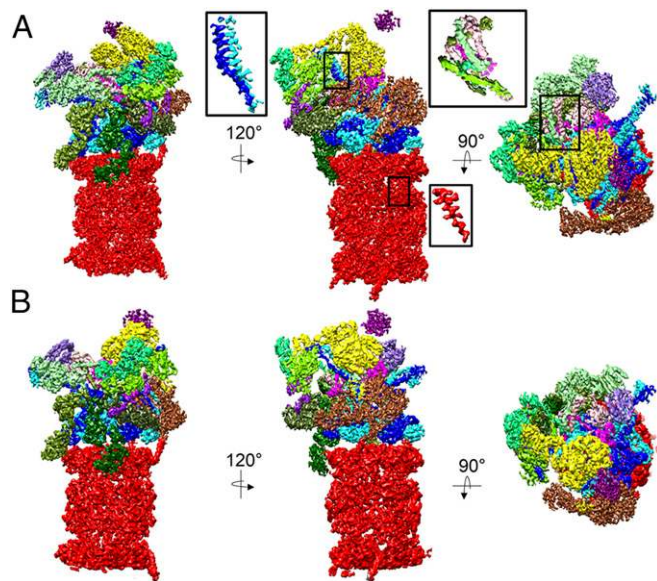
Fig. 1. Cryo-EM reconstructions of the yeast 26S proteasome in the s1 (*A*) and s2 (*B*) states at resolutions of 4.1 Å and 4.5 Å, respectively. The 26S proteasome is colored according to the subunits: CP (red); Rpt1, Rpt6, and Rpt4 (blue); Rpt2, Rpt3, and Rpt5 (cyan); Rpn1 (brown); Rpn2 (yellow); Rpn3, Rpn5, Rpn6, Rpn7, Rpn9, and Rpn12 (shades of green); and Rpn8, Rpn10, Rpn11, Rpn13, and Sem1 (shades of purple). (*Insets*) Selected magnified features of the s1 reconstruction: the coiled coil of Rpt3/6, α-helix of the CP, and helical bundle of the lid.
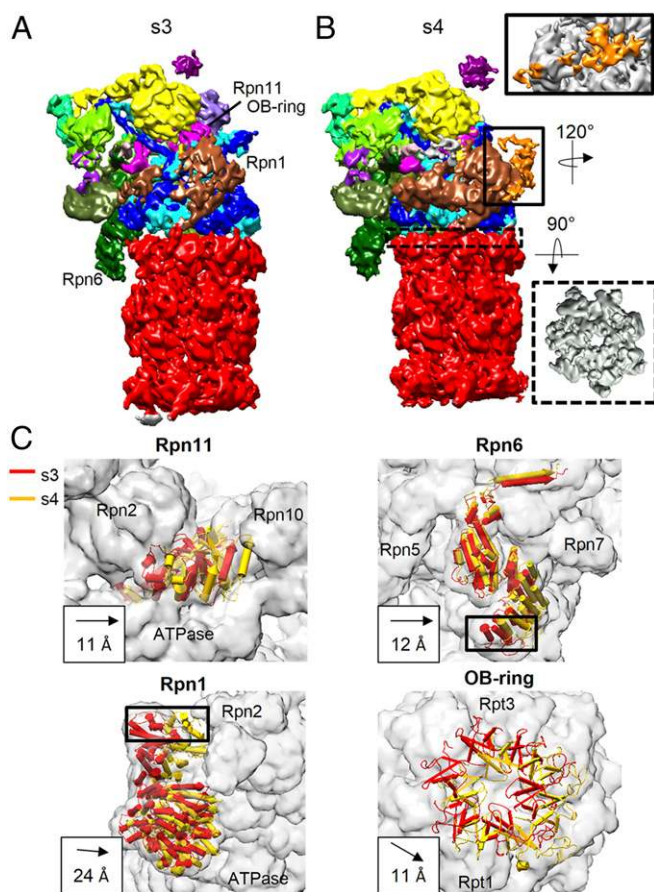
Fig. 2. Cryo-EM reconstructions of the yeast 26S proteasome in the s3 (*A*) and s4 (*B*) states at resolutions of 7.8 Å and 7.7 Å, respectively. The proteasome is colored according to the color code in Fig. 1. (*B, Insets*) Box outlined with a solid line shows the Ubp6 density low-pass-filtered to 10 Å (orange), and the box outlined with a dotted line shows a segmented density of the CP α-rings. (*C*) Comparison of selected subunits in the s3 and s4 states. The proteasome density of the s3 state is displayed in gray, and the s3 and s4 models of the subunits are colored in red and yellow, respectively.

AMP-PNP and ADP-BeF$_x$ are known as "nonhydrolyzable" nucleotide analogs that mimic an ATP ground state with tetrahedral geometry similar to the geometry of the "slowly hydrolyzable" nucleotide analog adenosine 5′-[γ-thio]triphosphate (ATP-γ-S) (29). Upon 3D classification, each dataset showed different abundances of the conformational states (Fig. S3*B*). Although the inhibition of the ATPase activity by AMP-PNP was weaker than for other analogs (Fig. S3*A*), the class averages of the AMP-PNP dataset showed exclusively the s3 conformation. In contrast, the presence of ADP alone led to highly heterogeneous conformations, which could not be classified into distinct states (Table S1). In the BeF$_x$ dataset, particles were distributed into four different classes (Fig. S3*B*). One of these classes showed a previously unobserved conformation of the 26S proteasome (Fig. 2*B* and Fig. S4), which we termed the s4 state. In the ADP-BeF$_x$ and ATP/BeF$_x$ samples, the occupancy of the s4 class was, respectively, 2% and 9%. After angular refinement, the s3 and s4 maps yielded resolutions of 7.8 Å and 7.7 Å, respectively (Fig. 2 *A* and *B* and Fig. S1*F*).

We modeled the s3 structure using MDFF to fit the s2 model into the s3 density, and the s4 structure based on the resulting s3 model (Fig. S3*C*). Secondary structure elements like α-helices were detected and positioned for all subunits. However, the low-resolution EM densities of the s3 and s4 states did not allow for the unambiguous identification of side chains.

Structural Features of the s4 Conformation. Although, overall, the s4 structure seems similar to the s3 structure, some subunits, such as Rpn1, Rpn6, Rpn11, and the AAA⁺ ATPase, adopt different conformations (Fig. 2C). For example, compared with the s3 conformer, the N-terminal α-solenoid of Rpn6 moves by ~12 Å toward Rpn7, independent of the overall rotation of the lid complex, whereas Rpn11 shifts by ~11 Å together with the entire oligosaccharide-binding (OB) ring. The rigid-body rotation of Rpn1 from s3 to s4 positions the Rpn1 N terminus ~24 Å closer to the AAA⁺ ring (Fig. S3 E and F). Compared with the s1 state, Rpn1 shifts and rotates in the s4 state, leading to an interaction of its N terminus with Rpt2 and Rpt6. This conformational change increases the distance between the central leucine-rich repeats domain of Rpn1 and the coiled coil of Rpt4/5, which might facilitate Ubp6 binding (Fig. S3F). Indeed, we observed an additional density between Rpn1 and the OB ring in the s4 state (Fig. 2B, box), which coincides with the position of Ubp6 (30). Further focused classification of the s4 dataset revealed that ~50% of the particles do not possess Ubp6 (Fig. S3D), roughly consistent with the amount of Ubp6 in the sample determined by MS.

HbYX Motifs and the Gate of the CP in the Four Different States. The diameter of the CP gate varies in the four observed conformations (Fig. S5). Consistent with previous studies (17, 26), the EM map of the CP in the s1 state shows high densities corresponding to the N termini of the α-subunits at the CP gate (Fig. S5 A and B). Interestingly, we observed no clear density within the central pore in the EM map of the s4 state (Fig. 2B, Inset, and Fig. S5 A and C), suggesting the opening of the CP gate. To quantify gate opening, we calculated the radial average of the EM density perpendicular to the CP axis (Fig. S5D). The normalized intensity of the s1 state is similar to the normalized intensity of the crystal structure of the CP with a closed gate [Protein Data Bank (PDB) ID code 5cz4 (31)] (Fig. S5 E and G). The s4 state shows the lowest normalized intensity at the center (Fig. S5K), in good agreement with the open-gate CP crystal structure [PDB ID code 1z7q (32)] (Fig. S5M). In the s4 model, several residues corresponding to the EM densities of the N-terminal extension are extended toward the RP (Fig. S5C), similar to the conformation observed in the CP–PA26 complex (32). The normalized intensities of s2 and s3 lie in between those extrema, indicating a partially closed gate (Fig. S5 H–J and M).

Next, we analyzed the density at the interface between the CP and RP. In contrast to the human 26S structures (22), all three HbYX motifs (Rpt2, Rpt3, and Rpt5) show clear densities inside the α-pockets in the four yeast conformational states (Fig. S6A). In the s1 structure, the conformation of the Rpt2 HbYX motif is similar to that of the HbYX motif of the proteasome-activating nucleotidase PAN in complex with the CP (11). The conserved tyrosine in the Rpt2 HbYX motif is in proximity to the arginine residue of the α4 subunit (Fig. S6B). In addition to the association of the HbYX motifs, in the s2 state, the Rpt1 C-terminal α-helix extends toward the C terminus of the α6 subunit (Fig. S6C). In the s4 state, in addition to the three HbYX motifs, the C-terminal tail of Rpt6 was detected at the interface between the α3 and α4 subunits (Fig. S6A).

Conformational Change of the AAA⁺ ATPase and the Pore Loops. In the s1 AAA⁺ ATPase, the OB and AAA⁺ rings are stacked on top of each other, but only the AAA⁺ ring forms a "lockwasher" conformation, in which the helical-shaped ring is split at the interface between Rpt6 and Rpt3 (17, 29). The large domains of the Rpt subunits are positioned at different heights. Rpt2 positions at the bottom and Rpt3 at the top (Fig. S7). The AAA⁺ ring is further right-handed twisted, arranging the α8 helices, which are C-terminal of the pore-1 loop in different orientations: Rpt2 and Rpt6 tilt inward up to 48°, and Rpt3 is almost planar with respect to the CP plane (Fig. 3). In this arrangement, the Rpt2 pore-1 loop is located closest to the CP and the Rpt3 pore-1 loop is proximal to the OB ring (Fig. 3 and Fig. S7).

Compared with the s1, in the s2 state the AAA⁺ ATPase shifts toward higher coaxial alignment with the CP, without significant local conformational changes (Fig. 3 and Figs. S4 and S7–S9), indicating that the coaxial alignment is not an ATP-driven conformational change. The AAA⁺ ring is rotated by ~8° and moved by ~17 Å for further coaxial alignment in the s3 state (Fig. S4). The large movement of the Rpt subunits relocates the opening of the lockwasher conformation to a site opposite of Rpt3/6, the interface of Rpt5/1. In this conformation, the α8 helices of Rpt1 and Rpt2 are tilted outward and Rpt4 and Rpt5 inward, resulting in a rearrangement of the pore-1 loop with Rpt5 at the bottom and Rpt1, Rpt2, and Rpt6 at the top (Fig. 3). Finally, the s4 AAA⁺ ring shows only a slight shift from the s3 conformation (Fig. S4). However, the lockwasher conformation, which splits at the interfaces between Rpt3/4 and Rpt4/5, is still preserved. In this conformation, the N termini of the α8 helices locate such that Rpt5 is at the top position and Rpt3 is at the bottom position. In all four conformational states, the AAA⁺ ATPase adopts different lockwasher conformations, which change the height of each pore-1 loop by switching the opening of the AAA⁺ ring.

Nucleotide-Binding Pocket and Nucleotide Binding. Like other AAA⁺ ATPase family members, the nucleotide-binding pocket is formed by five conserved motifs: Walker A, Walker B, sensor I, sensor II, and Arg-finger. The nucleotide is located at the "interface module," defined by a small domain of one Rpt subunit and the large domain of its clockwise adjacent Rpt subunit (20, 33). In the s1 state, the interface module units are closely connected to each other, except at the split site between Rpt6 and Rpt3 (Fig. 4D). Similar to previous studies (22, 24, 25), the s1 map shows density for nucleotides in all six nucleotide-binding pockets (Fig. 4 A, F, and G). However, only five of the six Arg-fingers are engaged in nucleotide binding ("engaged pocket"), in which the phosphates (Pi) of the nucleotide interact with the side chains of the two Arg residues of the Arg-finger (Fig. 4A). In the engaged pockets, the distance between the N-terminal tip of the α6 helix at the Walker A motif and the center of α10 helix located after the walker B motif ("pocket distance") is ~4–5 Å, showing tight ATP binding (Fig. 4 C and D). In contrast, the pocket distance of the interface module Rpt6/3 is ~30 Å (Fig. 4D). Interestingly, the Rpt3 Arg-fingers are projected away from the nucleotide-binding pocket and form hydrogen bonds with the carboxy groups of Rpt6, Glu140, and Val141 ("open pocket") (Fig. 4 A and C). Despite nonengagement of the Rpt3 Arg-finger, there is still nucleotide density in the Rpt6/3 pocket. Indeed, the density volume of the Rpt6/3 pocket is smaller than the nucleotide densities of the rest of the subunits, implying ADP binding (22). The conformations of the binding pockets in the s2 state are identical to the conformations of the binding pockets in the s1 state (Fig. 4 B and G), supporting the notion that there is no ATP hydrolysis involved in the conformational change from s1 to s2 (Figs. S8 and S9). Interestingly, we identified nucleotide densities in all Rpt subunits in both the s3 and s4 states (Fig. 4G). Similar to the s1/s2 states, the interface modules of the s3 and s4 states are in close contact with each other, except for the split sites, probably for tight ATP binding (Fig. 4 A–D). In the s3 state, the pocket distance of Rpt5/1, which is localized at the split site, is longer than the others (~28 Å), indicating a different coordination of the nucleotide from the coordination in the engaged pockets. In the s4 state, the pockets of two subunits, Rpt3/4 and Rpt4/5, are expanded (~21 Å) (Fig. 4D). Considering that the pocket distance probably corresponds to different nucleotide binding, the conformational changes between s2, s3, and s4 may reflect different nucleotide binding by the AAA⁺ ATPase.

Discussion

Here, we present four different conformational states of the yeast 26S proteasome obtained in the presence of different nucleotides and nucleotide analogs. One of the states represents a previously unobserved s4 conformation in which the lockwasher conformation of the AAA⁺ ATPase is rearranged to position the pore-1 loop differently from the three other known states. The four conformers provide insights into the functional cycle of the ATPase module
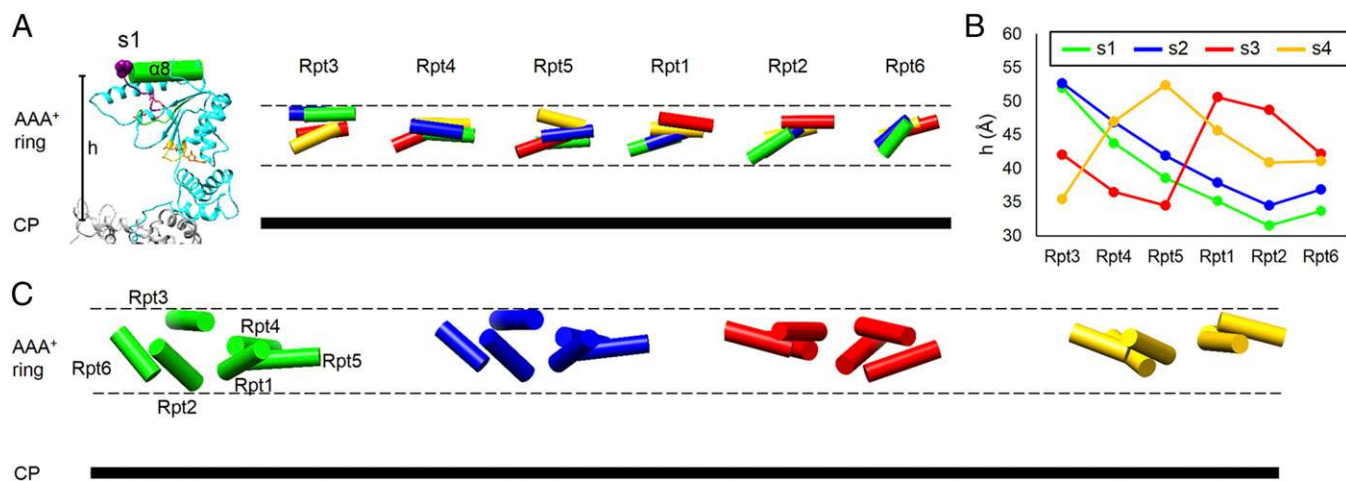
Fig. 3. Conformation of the AAA+ ATPase in the four states. (*A*) To visualize the arrangement of the pore-1 loops (purple, the conserved tyrosine residues are shown as spheres), the α8 helices of the Rpt subunits, which are C-terminal of the pore-1 loop, are depicted as cylinders (s1, green; s2, blue; s3, red; and s4, yellow). (*Left*) Each α8 helix of the Rpt subunits is shown individually in the same orientation with the Rpt3 structure in the s1 state (ribbon). (*B*) Height (h) of the N-terminal tip of the α8 helix with respect to the CP gate (plane spanning through the Cα atoms of α4 Arg-27, α2 Glu-30, and α6 Glu-30) is shown. (*C*) Conformation of the α8 helices of the four states.

and its role in substrate translocation: (*i*) The AAA+ ring changes the positions of the split site of the lockwasher conformation, which leads to rearrangements of the pore-1 loop; (*ii*) all six nucleotide-binding pockets are occupied, although the Arg-fingers are not engaged in all sites; (*iii*) the conformational change of the AAA+ ATPase is coupled with the CP gate opening; and (*iv*) three HbYX motifs constitutively bind to the α-pockets of the CP.

Substrate Translocation in the Lockwasher Conformation. The AAA+ ATPase family belongs to an additional strand catalytic glutamate (ASCE) superfamily, which includes RecA-like ATPases (33). Despite the high degree of structural conservation among the members of the ASCE superfamily (33), there are major differences in their hexameric assemblies. ClpX assembles into a closed planar ring but breaks symmetry by rotating the hinge region between the small and large domains of a subunit to form an "unloadable" conformation (34). The RecA ATPase DNA helicases, Rho and E1, also have a planar conformation, whereas DnaB6 is assembled into a lockwasher conformation (35). In the yeast 26S AAA+ ATPase, all four structures adopt a lockwasher conformation with different split sites. So far, the only planar conformation of the 26S proteasome was found in the presence of a model ubiquitylated substrate, in which the pore-1 loops were suggested to be arranged in a plane (36). In the substrate-engaged structure, the position of the AAA+ ring with respect to the CP is similar to the positions of the s3 and s4 conformers. However, the conformation of each Rpt subunit, including the arrangement of the pore-1 loop, is rather close to the s3 state. In the lockwasher conformation, the elongated pitch of the pore-1 loop may allow the ATPase to translocate polypeptides with a larger distance than the planar conformation. The distance between the top and bottom positions of the pore-1 loops of the 26S proteasome is ∼2 nm, almost double the ClpX substrate translocation step size (37). This finding indicates that the proteasome pore-1 loops in the staircase arrangement can likely translocate a polypeptide with a similar or even larger step size than ClpX.

In all reported conformations of the 26S proteasome, including the "open-gate" conformation (S_D conformation) (22–25), the AAA+ ATPase adopts a lockwasher conformation. However, we note that the lockwasher conformation of the AAA+ ATPase and the staircase arrangement of the pore-1 loops in the s4 state are not similar to the S_D conformation or any other reported conformation.

CP Gate-Opening Mechanisms. A previous structural study showed that insertion of the C-terminal HbYX motifs causes a conformational change for the CP gate opening concomitant with a rotation of the α-subunits (11). Although our s4 map shows no clear density in the pore region, probably representing an open-gate state, we did not observe any significant rotation of the α-subunits: Only the N-terminal extensions turn up toward the RP, as seen in the PA26–CP complex (38). In contrast, a strong density within the gate in the s1 state (Fig. S5*A*) suggests a closed gate. In the s2 and s3 states, the normalized intensity within the gate is between the normalized intensities of s1 and s4, indicating incomplete gate opening. In the crystal structure of the CP with the proteasome activator Blm10, the N-terminal extensions were not in the closed conformation but did not show a clear density, suggesting a "partial closed-gate" (10). The gate conformation of the s2 and s3 states may be similar to such a partial closed-gate state. Considering the elasticity of an unfolded polypeptide (39), the partial closed-gate may hinder the diffusion of the translocated polypeptide by gripping it with the N-terminal extensions. In addition, the fact that all four states exhibit densities of three HbYX motifs in the α-pockets but only the s4 conformation adopts an open-gate conformation, suggests that HbYX engagement is not sufficient to open the gate for the yeast 26S proteasome.

The reported S_D conformation of the human 26S proteasome showed a reduced density within the gate. However, analysis of the normalized intensity of the S_D conformation (Fig. S5*L*) shows that the gate area is rather similar to the s3 state (Fig. S5*O*), implying that the S_D state represents a conformation different from the s4 state. In the S_D conformation, two additional C-terminal tails (Rpt1 and Rpt6), together with insertion of the three HbYX motifs into the α-pockets, were suggested to trigger CP gate opening (25). However, only the C-terminal tail of Rpt6 was detected in the map of the s4 state (Fig. S6*A*). Due to the relatively low resolution of the s4 and S_D states, it is unclear whether this difference is due to a different gate-opening mechanism in yeast and humans or to different interpretation of the EM maps.

Functional Model. Mechanochemical studies of ClpX have revealed that a conformational change of the pore-1 loop is coupled with Pi release to power translocation (39). In addition, among the six promoters, a subunit whose pore-1 loop is in direct contact with a translocated polypeptide may have a higher probability of hydrolyzing ATP first (40), indicating that an Rpt subunit at the top of the staircase may hydrolyze first. Interestingly, the pore-1 loop of the Rpt subunit at the top of the staircase is adjacent to the Rpt

Fig. 4. Comparison of the nucleotide-binding pockets of the AAA+ ATPase in the s1 (*A*) and s2 (*B*) states. Nucleotide-binding pockets with modeled nucleotides (orange), neighboring Arg-fingers (red), the Walker A motif (yellow), and the Walker B motif (green) of the Rpts (Rpt2, Rpt3, and Rpt5 are colored cyan, and Rpt1, Rpt4, and Rpt6 are colored blue) are shown. (*C*) Close-up view of the model of an engaged pocket and an open pocket in the s1 state, showing the position of the helices α6 and α10. (*D*) Pocket distance of the N-terminal tip of α6 and the center of α10 for all nucleotide-binding pockets and states. (*E*) Histogram of the pocket distances from *D*. (*F*) Subtraction of the simulated map of the AAA+ ring of the ATPase model (without nucleotides) from the experimental EM map of the s1 state. (*G*) Comparison of difference maps calculated as described in *F* for all four states.

subunit with an open nucleotide-binding pocket, in which the pore-1 loop is located at the bottom of the staircase.

Based on our structures, we propose the following functional model of the 26S proteasome (Fig. S10). In the absence of substrate, the proteasome is present in the ground state (s1), which represents the lowest energy conformation of the four states. When the proteasome is activated, most likely by substrate binding, it undergoes a conformational change from the ground state to the translocation-competent states (s2–s4). Because no structural change is observed in the AAA+ ring between s1 and s2, this transition is most likely not ATP-dependent. The translocation of substrates may be initiated by Rpt3, whose pore-1 loop is at the top position of the staircase in the s2 state. Polypeptide binding to the Rpt3 pore-1 loop may trigger ATP hydrolysis, probably followed by Pi release. The Pi release from the Rpt3/4 pocket brings the Rpt3 pore-1 loop to the bottom of the staircase. As a consequence, the pockets of the neighboring subunits (Rpt3/4 and Rpt4/5) undergo a conformational change, resulting in the relocation of the Rpt5 pore-1 loop at the top position (s4). A concerted conformational change occurs to open the CP gate, which allows substrate translocation into the CP antechamber. Coupling the gate opening with ATP hydrolysis prevents the polypeptide from slipping back. In a similar manner, the Rpt5 pore-1

loop undergoes a conformational change coupled with Pi release to be located at the bottom of the staircase (s3), again powering the work for the translocation. It is very likely that there exists more states than the four discussed here, in which the nucleotide pockets of Rpt1/2 and 2/6 are open. We assume that the cycle continues until the substrate translocation process is finished. Our structures favor a model in which the hydrolysis cycle occurs in a sequential order around the ring rather than in a stochastic manner.

Materials and Methods

Purification and Characterization of 26S Proteasome. Yeast 26S proteasomes were isolated from *Saccharomyces cerevisae* by affinity purification using the 3× FLAG-tagged subunit Rpn11. Different ATP analogs were introduced during or after the sucrose gradient purification step (*SI Materials and Methods*). Samples (~1 mg/mL) were stored at −80 °C until further use.

Data Acquisition and Image Processing. All datasets were collected on a Titan Krios with a direct electron detector in movie mode. The pixel size at the specimen level was 1.35 Å for Falcon cameras and 1.38 Å for the K2 camera (*SI Materials and Methods*). Both single-capped 26S and double-capped particles were used in all datasets for classification and to obtain the final reconstructions (*SI Materials and Methods*). All image processing steps were carried out in TOM (41) and RELION (42).

Model Building. Initial models were obtained by comparative and de novo modeling (*SI Materials and Methods*). The initial structure for the s1 state was the merged structure of the CP crystal structure [PDB ID code 5cz4 (31)] and the RP homology model based on the human structure [PDB ID code 5l4g (22)]. The subunits were positioned into the EM map and subsequently refined. Real-space refinement was first performed as described by Goh et al. (43) using MDFF (27) and then in reciprocal space. MDFF simulations were prepared using QwikMD (44), analyzed with VMD (45), and carried out with NAMD (46). The refined final structure of s1 was used to initiate an MDFF run into the density of the s2 state. The final refined structure of the s2 state was fitted through MDFF into the density of the s3 state, and the final s3 state structure was finally fitted into the s4 density.

1. Hershko A, Ciechanover A, Varshavsky A (2000) Basic Medical Research Award. The ubiquitin system. *Nat Med* 6(10):1073–1081.
2. Voges D, Zwickl P, Baumeister W (1999) The 26S proteasome: A molecular machine designed for controlled proteolysis. *Annu Rev Biochem* 68:1015–1068.
3. Finley D (2009) Recognition and processing of ubiquitin-protein conjugates by the proteasome. *Annu Rev Biochem* 78:477–513.
4. Peters JM, Cejka Z, Harris JR, Kleinschmidt JA, Baumeister W (1993) Structural features of the 26 S proteasome complex. *J Mol Biol* 234(4):932–937.
5. Pühler G, et al. (1992) Subunit stoichiometry and three-dimensional arrangement in proteasomes from Thermoplasma acidophilum. *EMBO J* 11(4):1607–1616.
6. Seemüller E, et al. (1995) Proteasome from Thermoplasma acidophilum: A threonine protease. *Science* 268(5210):579–582.
7. Groll M, et al. (1997) Structure of 20S proteasome from yeast at 2.4 A resolution. *Nature* 386(6624):463–471.
8. Baumeister W, Walz J, Zühl F, Seemüller E (1998) The proteasome: Paradigm of a self-compartmentalizing protease. *Cell* 92(3):367–380.
9. Smith DM, et al. (2007) Docking of the proteasomal ATPases' carboxyl termini in the 20S proteasome's alpha ring opens the gate for substrate entry. *Mol Cell* 27(5):731–744.
10. Sadre-Bazzaz K, Whitby FG, Robinson H, Formosa T, Hill CP (2010) Structure of a Blm10 complex reveals common mechanisms for proteasome binding and gate opening. *Mol Cell* 37(5):728–735.
11. Yu Y, et al. (2010) Interactions of PAN's C-termini with archaeal 20S proteasome and implications for the eukaryotic proteasome-ATPase interactions. *EMBO J* 29(3):692–702.
12. Shi Y, et al. (2016) Rpn1 provides adjacent receptor sites for substrate binding and deubiquitination by the proteasome. *Science* 351(6275):aad9421.
13. Husnjak K, et al. (2008) Proteasome subunit Rpn13 is a novel ubiquitin receptor. *Nature* 453(7194):481–488.
14. Deveraux Q, Ustrell V, Pickart C, Rechsteiner M (1994) A 26 S protease subunit that binds ubiquitin conjugates. *J Biol Chem* 269(10):7059–7061.
15. Verma R, et al. (2002) Role of Rpn11 metalloprotease in deubiquitination and degradation by the 26S proteasome. *Science* 298(5593):611–615.
16. Yao T, Cohen RE (2002) A cryptic protease couples deubiquitination and degradation by the proteasome. *Nature* 419(6905):403–407.
17. Lander GC, et al. (2012) Complete subunit architecture of the proteasome regulatory particle. *Nature* 482(7384):186–191.
18. Lasker K, et al. (2012) Molecular architecture of the 26S proteasome holocomplex determined by an integrative approach. *Proc Natl Acad Sci USA* 109(5):1380–1387.
19. Sauer RT, Baker TA (2011) AAA+ proteases: ATP-fueled machines of protein destruction. *Annu Rev Biochem* 80:587–612.
20. Nyquist K, Martin A (2014) Marching to the beat of the ring: Polypeptide translocation by AAA+ proteases. *Trends Biochem Sci* 39(2):53–60.
21. Unverdorben P, et al. (2014) Deep classification of a large cryo-EM dataset defines the conformational landscape of the 26S proteasome. *Proc Natl Acad Sci USA* 111(15):5544–5549.
22. Schweitzer A, et al. (2016) Structure of the human 26S proteasome at a resolution of 3.9 Å. *Proc Natl Acad Sci USA* 113(28):7816–7821.
23. Luan B, et al. (2016) Structure of an endogenous yeast 26S proteasome reveals two major conformational states. *Proc Natl Acad Sci USA* 113(10):2642–2647.
24. Huang X, Luan B, Wu J, Shi Y (2016) An atomic structure of the human 26S proteasome. *Nat Struct Mol Biol* 23(9):778–785.
25. Chen S, et al. (2016) Structural basis for dynamic regulation of the human 26S proteasome. *Proc Natl Acad Sci USA* 113(46):12991–12996.
26. Beck F, et al. (2012) Near-atomic resolution structural model of the yeast 26S proteasome. *Proc Natl Acad Sci USA* 109(37):14870–14875.
27. Trabuco LG, Villa E, Schreiner E, Harrison CB, Schulten K (2009) Molecular dynamics flexible fitting: A practical guide to combine cryo-electron microscopy and X-ray crystallography. *Methods* 49(2):174–180.
28. Chen X, Lee BH, Finley D, Walters KJ (2010) Structure of proteasome ubiquitin receptor hRpn13 and its activation by the scaffolding protein hRpn2. *Mol Cell* 38(3):404–415.
29. Śledź P, et al. (2013) Structure of the 26S proteasome with ATP-γS bound provides insights into the mechanism of nucleotide-dependent substrate translocation. *Proc Natl Acad Sci USA* 110(18):7264–7269.
30. Aufderheide A, et al. (2015) Structural characterization of the interaction of Ubp6 with the 26S proteasome. *Proc Natl Acad Sci USA* 112(28):8626–8631.
31. Huber EM, et al. (2016) A unified mechanism for proteolysis and autocatalytic activation in the 20S proteasom. *Nat Commun* 7:10900.
32. Förster A, Masters EI, Whitby FG, Robinson H, Hill CP (2005) The 1.9 A structure of a proteasome-11S activator complex and implications for proteasome-PAN/PA700 interactions. *Mol Cell* 18(5):589–599.
33. Wendler P, Ciniawsky S, Kock M, Kube S (2012) Structure and function of the AAA+ nucleotide binding pocket. *Biochim Biophys Acta* 1823(1):2–14.
34. Glynn SE, Martin A, Nager AR, Baker TA, Sauer RT (2009) Structures of asymmetric ClpX hexamers reveal nucleotide-dependent motions in a AAA+ protein-unfolding machine. *Cell* 139(4):744–756.
35. Itsathitphaisarn O, Wing RA, Eliason WK, Wang J, Steitz TA (2012) The hexameric helicase DnaB adopts a nonplanar conformation during translocation. *Cell* 151(2):267–277.
36. Matyskiela ME, Lander GC, Martin A (2013) Conformational switching of the 26S proteasome enables substrate degradation. *Nat Struct Mol Biol* 20(7):781–788.
37. Liu S, Chistol G, Bustamante C (2014) Mechanical operation and intersubunit coordination of ring-shaped molecular motors: Insights from single-molecule studies. *Biophys J* 106(9):1844–1858.
38. Whitby FG, et al. (2000) Structural basis for the activation of 20S proteasomes by 11S regulators. *Nature* 408(6808):115–120.
39. Sen M, et al. (2013) The ClpXP protease unfolds substrates using a constant rate of pulling but different gears. *Cell* 155(3):636–646.
40. Martin A, Baker TA, Sauer RT (2008) Diverse pore loops of the AAA+ ClpX machine mediate unassisted and adaptor-dependent recognition of ssrA-tagged substrates. *Mol Cell* 29(4):441–450.
41. Nickell S, et al. (2005) TOM software toolbox: Acquisition and analysis for electron tomography. *J Struct Biol* 149(3):227–234.
42. Scheres SH (2012) RELION: Implementation of a Bayesian approach to cryo-EM structure determination. *J Struct Biol* 180(3):519–530.
43. Goh BC, et al. (2016) Computational methodologies for real-space structural refinement of large macromolecular complexes. *Annu Rev Biophys* 45:253–278.
44. Ribeiro JV, et al. (2016) QwikMD-integrative molecular dynamics toolkit for novices and experts. *Sci Rep* 6:26536.
45. Humphrey W, Dalke A, Schulten K (1996) VMD: Visual molecular dynamics. *J Mol Graph* 14(1):33–38.
46. Phillips JC, et al. (2005) Scalable molecular dynamics with NAMD. *J Comput Chem* 26(16):1781–1802.
47. Cox J, et al. (2014) Accurate proteome-wide label-free quantification by delayed normalization and maximal peptide ratio extraction, termed MaxLFQ. *Mol Cell Proteomics* 13(9):2513–2526.
48. Bartolommei G, Moncelli MR, Tadini-Buoninsegni F (2013) A method to measure hydrolytic activity of adenosinetriphosphatases (ATPases). *PLoS One* 8(3):e58615.
49. Korinek A, Beck F, Baumeister W, Nickell S, Plitzko JM (2011) Computer controlled cryo-electron microscopy–TOM² a software package for high-throughput applications. *J Struct Biol* 175(3):394–405.
50. Grant T, Grigorieff N (2015) Automatic estimation and correction of anisotropic magnification distortion in electron microscopes. *J Struct Biol* 192(2):204–208.
51. Li X, et al. (2013) Electron counting and beam-induced motion correction enable near-atomic-resolution single-particle cryo-EM. *Nat Methods* 10(6):584–590.
52. Mindell JA, Grigorieff N (2003) Accurate determination of local defocus and specimen tilt in electron microscopy. *J Struct Biol* 142(3):334–347.
53. Pettersen EF, et al. (2004) UCSF Chimera–a visualization system for exploratory research and analysis. *J Comput Chem* 25(13):1605–1612.
54. Bohn S, et al. (2010) Structure of the 26S proteasome from Schizosaccharomyces pombe at subnanometer resolution. *Proc Natl Acad Sci USA* 107(49):20992–20997.
55. Sali A, Blundell TL (1993) Comparative protein modelling by satisfaction of spatial restraints. *J Mol Biol* 234(3):779–815.
56. He J, et al. (2012) The structure of the 26S proteasome subunit Rpn2 reveals its PC repeat domain as a closed toroid of two concentric α-helical rings. *Structure* 20(3):513–521.
57. Mackerell AD, Jr, Feig M, Brooks CL, 3rd (2004) Extending the treatment of backbone energetics in protein force fields: Limitations of gas-phase quantum mechanics in reproducing protein conformational distributions in molecular dynamics simulations. *J Comput Chem* 25(11):1400–1415.
58. Stone JE, McGreevy R, Isralewitz B, Schulten K (2014) GPU-accelerated analysis and visualization of large structures solved by molecular dynamics flexible fitting. *Faraday Discuss* 169:265–283.
59. Greber BJ, et al. (2014) The complete structure of the large subunit of the mammalian mitochondrial ribosome. *Nature* 515(7526):283–286.
60. Adams PD, et al. (2002) PHENIX: Building new software for automated crystallographic structure determination. *Acta Crystallogr D Biol Crystallogr* 58(Pt 11):1948–1954.
61. Emsley P, Lohkamp B, Scott WG, Cowtan K (2010) Features and development of Coot. *Acta Crystallogr D Biol Crystallogr* 66(Pt 4):486–501.